



Simplify your imaging workflows

**Make research imaging workflows accessible, traceable,
and secure with Athena Software for Core Imaging Facilities.**

Thermo Scientific™ Athena Software is a premium imaging data management platform designed for core imaging facilities that support materials science research.

Athena Software ensures traceability of images, metadata, and experimental workflows through an intuitive and collaborative web interface.

Find out more at thermofisher.com/athena

ThermoFisher
SCIENTIFIC

Boosted Responsivity and Tunable Spectral Response in B-Site Substituted 2D $\text{Ca}_2\text{Nb}_{3-x}\text{Ta}_x\text{O}_{10}$ Perovskite Photodetectors

Xinya Liu, Siyuan Li, Ziqing Li, Yong Zhang, Wei Yang, Ziliang Li, Hui Liu, Dmitry V. Shtansky, and Xiaosheng Fang*

2D Dion-Jacobson perovskite oxides, featuring fascinating optical and electric properties, exhibit great potential in optoelectronic devices. However, the device sensitivity and spectral selectivity are limited. Herein, B-site substituted calcium niobate $\text{Ca}_2\text{Nb}_{3-x}\text{Ta}_x\text{O}_{10}$ ($x = 0, 0.5, 1, 1.5$) nanosheets are prepared by liquid exfoliation. The photodetectors (PDs) based on these nanosheets exhibit tunable spectral response by tailoring the band gap of the nanosheets. All the Ta-substituted PDs show increased photocurrent and enhanced responsivity, among which the $\text{Ca}_2\text{Nb}_{2.5}\text{Ta}_{0.5}\text{O}_{10}$ PD exhibits the optimal performance with a photocurrent of $31.4 \mu\text{A}$, a high on–off ratio of 5.6×10^4 and a boosted responsivity of 469.5 A W^{-1} at 1.0 V toward 295 nm , which is over 7000-fold higher than that of pristine $\text{Ca}_2\text{Nb}_3\text{O}_{10}$ PD. It is proposed that the significantly optimized responsivity is ascribed to the enhanced photoconductive gain that mainly originates from the introduction of the trap states by the B-site substitution. Nevertheless, excess substitution is detrimental to the responsivity and the response speed. This work demonstrates that the rational control of B-site substitution tailors the band gap and modulates the charge-carrier behaviors in 2D perovskite oxides, which provides an effective avenue for achieving high-performance PDs with tunable spectral response and excellent responsivity.


high-temperature superconductivity,^[3] giant magnetoresistance,^[4] ferroelectricity,^[5] photocatalytic activity.^[6] In recent years, with the development of 2D materials, interest in this layer structured material has been aroused again for its potential in being transformed into a 2D nanosheet geometry. A multistep soft-chemical exfoliation technique has been well developed to delaminate these layered perovskites into their elementary layer units to obtain nanosheets.^[7,8] It is found that the ultrathin thickness and large specific area of nanosheets can bring perovskites some attractive optical, photochemical, or electric properties (e.g., high photoluminescence efficiency, large photoconductive gain, etc.), which expands their potential for fabricating devices with various photo-induced functionalities such as solar cells^[9–12] and light-emitting diodes,^[13,14] as well as high-performance photodetectors (PDs).^[15,16]

2D DJ perovskites have been extensively studied in the photocatalysis field due to their outstanding photocatalytic activity for water splitting under ultraviolet or visible light. For instance, the photochemical water splitting activity of $\text{H}\text{Ca}_2\text{Nb}_3\text{O}_{10}$ nanosheets for H_2 evolution under the irradiation of a Hg lamp have been reported, and it is also found that loading Pt nanoparticles on nanosheets could increase the hydrogen production.^[17] The charge carrier trapping and recombination process in exfoliated $\text{Ca}_2\text{Nb}_3\text{O}_{10}$ nanosheet has already been characterized to reveal the ultrafast carrier dynamics in this material.^[18] On the basis of photocatalytic studies on the band gap and photogenerated carrier dynamics of these niobate nanosheets, researchers begin to turn their eyes on expanding its application in UV PDs. Our group has systematically investigated the UV photodetector based on individual $\text{Sr}_2\text{Nb}_3\text{O}_{10}$ nanosheet. The PD exhibit excellent performance with a responsivity up to 1200 A W^{-1} , an EQE of $5.6 \times 10^5\%$, a detectivity of 1.4×10^{14} Jones and fast response speed ($t_{\text{rise}} = 0.4 \text{ ms}$, $t_{\text{decay}} = 40 \text{ ms}$).^[15] Besides, the UV PD based on 2D $\text{Ca}_2\text{Nb}_3\text{O}_{10}$, another important member of DJ perovskites family, has also been reported, which possesses faster response speed ($t_{\text{rise}} = 0.08 \text{ ms}$, $t_{\text{decay}} = 5.6 \text{ ms}$) compared to the 2D $\text{Sr}_2\text{Nb}_3\text{O}_{10}$ PD, nevertheless, an inferior responsivity instead.^[19] Especially for the $\text{Ca}_2\text{Nb}_3\text{O}_{10}$ nanosheet film-based PD, there is much room

1. Introduction

The layered Dion-Jacobson (DJ) perovskite oxides, with the formula of $A'[\text{A}_{n-1}\text{B}_n\text{O}_{3n+1}]$, where A' , A , B represent alkali metal, alkaline earth metal, transition metal ions respectively, consist of negatively charged octahedral BO_6 slabs and cations in the interlayer space.^[1] Since being discovered nearly 3 decades ago, such perovskite oxides attracted extensive attention due to their intriguing physical and chemical properties,^[2] such as

X. Y. Liu, S. Y. Li, Dr. Z. Q. Li, Dr. Y. Zhang, W. Yang, Dr. Z. L. Li, Dr. H. Liu, Prof. X. S. Fang
Department of Materials Science
Fudan University
Shanghai 200433, P. R. China
E-mail: xshfang@fudan.edu.cn
Prof. D. V. Shtansky
National University of Science and Technology “MISIS”
Moscow 119049, Russia

 The ORCID identification number(s) for the author(s) of this article can be found under <https://doi.org/10.1002/adfm.202101480>.

DOI: 10.1002/adfm.202101480

for the improvement in its responsivity, a key parameter indicating the response sensitivity of a photodetector to optical signals. Thus, the optimization of the responsivity of the $\text{Ca}_2\text{Nb}_3\text{O}_{10}$ based PD can be a breakthrough to achieve PD with outstanding photoresponse sensitivity and more comprehensive performance. More importantly, the photoelectric behaviors of 2D perovskite oxides should be further investigated and revealed, which will promote its application in photodetection fields.

It is well known that defect engineering is a promising route for achieving an enhanced responsivity of the PDs. Generally, microstructural defects in semiconducting crystals may act as recombination or trapping centers, which are typically regarded as unfavorable factors in the optoelectronic devices. However, the inherent ability to influence the carrier dynamics of the defects if utilized appropriately may induce unexpected photoelectric behaviors (e.g., ultrafast response speed, ultrahigh responsivity, etc.) in photodetectors.^[20] Thus, many studies apply defect engineering to fabricate high-performance photodetectors.^[21] Normally, the defect engineering applied on conventional semiconductor is limited to the surface/interface treatment due to their thickness in the third dimension. While for 2D materials, the ultrathin thickness makes them essentially an interface-type material, which provides more space for the modulation of electronic properties through defect engineering.^[22] The regulation of photoresponse in reduced graphene oxide phototransistors through controlling the oxygenous defects has been realized. The defects acting as trapping centers in graphene influences the photocarrier transport and recombination and contributes to the high photoconductive gain, which results in the enhanced responsivity in phototransistor.^[23] The introduction of a stable trap effect, which can capture holes, in 2D $\text{MoS}_{2-x}\text{Se}_{2-2x}$ via synergistic effect of sulfur vacancies and substitutional Se atoms has been reported to be conducive to achieving ultrahigh photoresponsivity.^[20] Overall, regulation of the defects can be an effective way for optimizing the photoresponse sensitivity of the PD based on 2D materials.^[22] Heteroatom incorporation, as a strategy of defect engineering,^[24] can be applied to regulate defects in the $\text{Ca}_2\text{Nb}_3\text{O}_{10}$ nanosheets. Several researchers have reported the successful incorporation of extrinsic atoms into the $\text{Ca}_2\text{Nb}_3\text{O}_{10}$ nanosheets lattice by substituting the B-site cation.^[25–27] It is revealed that the B-site cation substitution can induce structural distortion and thus inevitably influence the electronic properties of the material.^[28] The introduced B-site heteroatoms have the possibility to act as carrier trap centers, which would remarkably influence the charge-carrier behaviors in the material.^[27] Therefore, it is possible to achieve the regulation of the photoelectric properties in the $\text{Ca}_2\text{Nb}_3\text{O}_{10}$ nanosheets to acquire improved photoresponse responsivity by applying defect engineering strategy through a B-site substitution method. Besides, the band structure of this d^0 transition metal perovskite oxides is significantly dependent on the B-site transition metal ion.^[28] The substitution of Ta for Nb on the B-site of $\text{Ca}_2\text{Nb}_3\text{O}_{10}$ nanosheets were once prepared and the tunable band edge potentials induced by the composition change was confirmed experimentally and computationally.^[25,26] Since the band gap of the materials determines the cutoff wavelength of PDs, this strategy also provides a possibility on regulating the spectral response of the PD. Therefore, the B-site substitution method,

through modulating the crystal structure and the related physicochemical properties of the perovskite oxides, exhibits great potential in tailoring the photoelectric properties and the band gap to fabricate the highly sensitive PD we pursuit.

In this work, B-site cation Nb^{5+} of $\text{Ca}_2\text{Nb}_3\text{O}_{10}$ are partially substituted by Ta^{5+} to form solid solution $\text{Ca}_2\text{Nb}_{3-x}\text{Ta}_x\text{O}_{10}$ with various Ta content ($x = 0, 0.5, 1, 1.5$). The nanosheets are prepared through high-temperature calcination and subsequent multistep soft chemical exfoliation method. Several characterization methods are applied to illustrate the morphology, crystallinity, and chemical composition of these nanosheets. The optical properties of the material exhibit a tunable band gap via controlling the Ta content. The photodetecting performance of the B-site substituted 2D $\text{Ca}_2\text{Nb}_3\text{O}_{10}$ based PDs can be significantly affected by the Ta content. The PDs display tunable spectral response and enhanced responsivity, among which the $\text{Ca}_2\text{Nb}_{2.5}\text{Ta}_{0.5}\text{O}_{10}$ PD exhibits the most outstanding performance with a boosted responsivity of 469.5 A W^{-1} at 1.0 V bias under 295 nm illumination, which is over 7000-fold higher than that of the PD based on pristine $\text{Ca}_2\text{Nb}_3\text{O}_{10}$. We propose that the enhanced responsivity can be ascribed to the high photoconductive gain that mainly originates from the introduction of the trap states by the B-site substitution. Nevertheless, the excess substitution is detrimental to the responsivity, as well as the response speed, considering the carrier scattering and the crystal character of the material. Therefore, the $\text{Ca}_2\text{Nb}_{2.5}\text{Ta}_{0.5}\text{O}_{10}$ PD outperforms other samples due to its suitable composition ratio, exhibiting the optimal responsivity and an acceptable response speed simultaneously. The results demonstrate the rational design of B-site cation substitution an effective route to achieve tunable spectral response and improve the photoresponse in 2D perovskite oxides-based PDs.

2. Results and Discussion

The $\text{Ca}_2\text{Nb}_{3-x}\text{Ta}_x\text{O}_{10}$ ($x = 0, 0.5, 1, 1.5$) nanosheets are prepared through a solid-state reaction and a subsequent multistep soft-chemical exfoliation method. **Figure 1** and Figure S1, Supporting Information, display the morphology of the intermediate products and the obtained $\text{Ca}_2\text{Nb}_{3-x}\text{Ta}_x\text{O}_{10}$ nanosheets, characterized by scanning electron microscopy (SEM) and atomic force microscopy (AFM). In the solid state reaction process, bulk metal oxide $\text{KCa}_2\text{Nb}_{3-x}\text{Ta}_x\text{O}_{10}$ precursors are well-crystallized via high-temperature calcination, with a distinct layered structure (Figure 1a), which makes the subsequent exfoliation possible. The soft-chemical exfoliation method includes two steps, that is, proton exchange in nitric acid and reaction with organic base tetra (*n*-butyl) ammonium hydroxide (TBA^+OH^-). In the proton exchange process, protonic $\text{HCa}_2\text{Nb}_{3-x}\text{Ta}_x\text{O}_{10}$ samples are obtained by replacing the K^+ with H^+ in the interlayer space, as presented in Figure 1b. Subsequently, the ion-exchange reaction between the H^+ and TBA^+OH^- expands the oxide layers infinitely, leading to the exfoliation of perovskite slabs ($\text{Ca}_2\text{Nb}_{3-x}\text{Ta}_x\text{O}_{10}$) into elementary nanosheets (Figure 1c–f). The SEM images reveal that the lateral size of nanosheets is distributed around 1 μm , independent of the composition ratio. The thickness of the nanosheets for all the $\text{Ca}_2\text{Nb}_{3-x}\text{Ta}_x\text{O}_{10}$ samples ranges

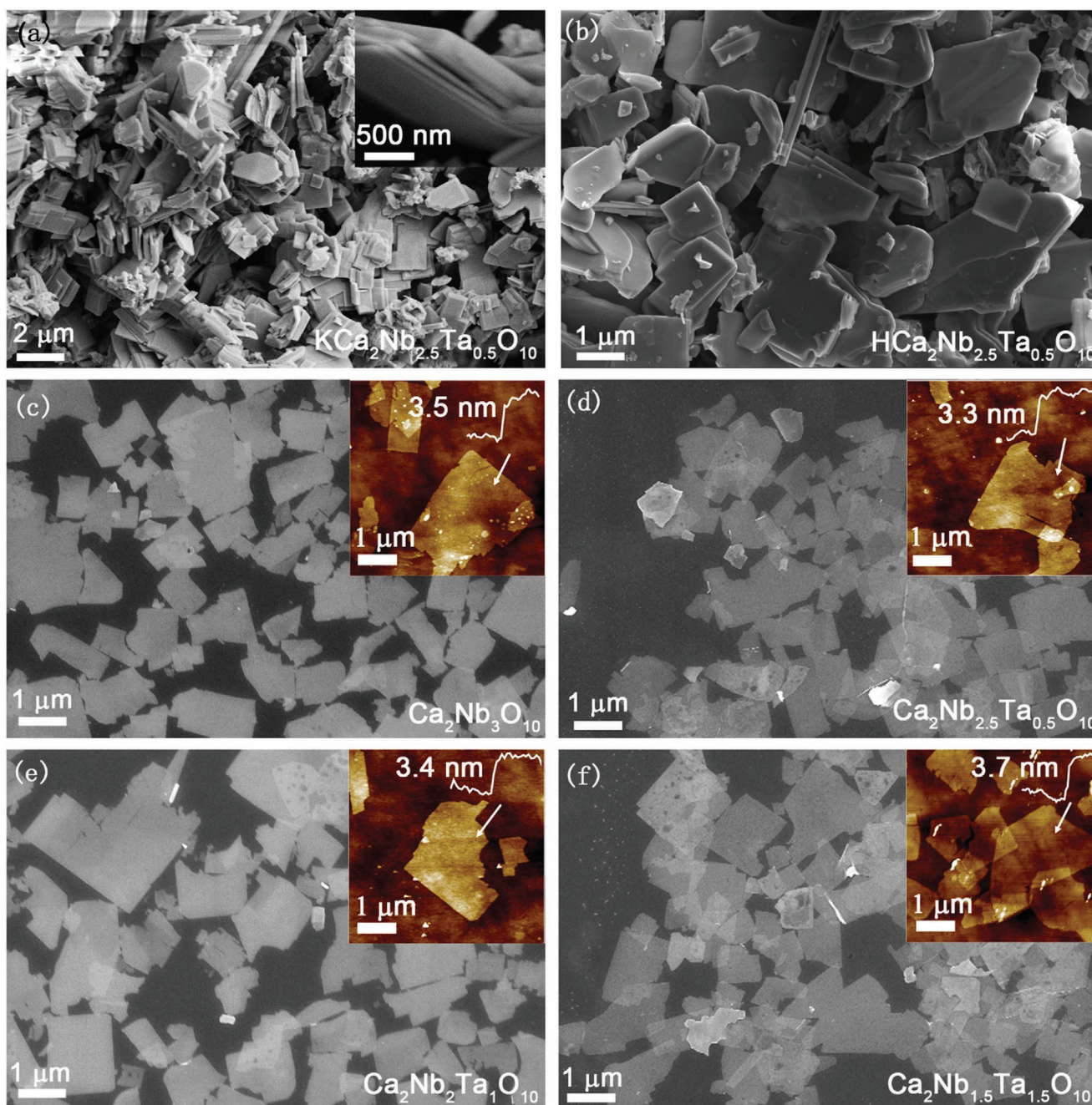


Figure 1. Morphological characterization of the $\text{Ca}_2\text{Nb}_{3-x}\text{Ta}_x\text{O}_{10}$ nanosheets ($x = 0, 0.5, 1, 1.5$). a) SEM image of the $\text{KCa}_2\text{Nb}_{2.5}\text{Ta}_{0.5}\text{O}_{10}$ precursor after solid state reaction, the inset showing the layered structure of the precursor. b) SEM image of proton exchanged product $\text{HCa}_2\text{Nb}_{2.5}\text{Ta}_{0.5}\text{O}_{10}$. c–f) SEM images of exfoliated $\text{Ca}_2\text{Nb}_{3-x}\text{Ta}_x\text{O}_{10}$ nanosheets, the insets displaying the typical AFM images with height profiles.

from 1 to 20 nm, as shown in the statistic thickness distribution (Figure S2, Supporting Information). It is reported that the monolayer of the $\text{Ca}_2\text{Nb}_3\text{O}_{10}$ nanosheet is ≈ 1.8 nm, and the thickness of 2D DJ perovskites depends on its layer number.^[19,29] Notably, for all the four $\text{Ca}_2\text{Nb}_{3-x}\text{Ta}_x\text{O}_{10}$ samples, the thickness values distribute intensively around several discrete numbers (e.g., 1.8, 3.6 nm, etc.), which experimentally confirms the layered nature of nanosheets. The inset pictures of Figure 1c–f present typical AFM images of two-layer

$\text{Ca}_2\text{Nb}_{3-x}\text{Ta}_x\text{O}_{10}$ ($x = 0, 0.5, 1, 1.5$) nanosheets, and the thickness are measured as 3.5, 3.3, 3.4, and 3.7 nm, respectively. No obvious morphological difference can be observed when comparing the morphology of the pristine and Ta-substituted $\text{Ca}_2\text{Nb}_3\text{O}_{10}$ nanosheets, implying that the substitution of Ta for Nb in a certain content has no clear influence on the morphological characteristics of the nanosheets.

X-ray diffraction (XRD) is employed to investigate the crystal phase structure of the obtained products. The XRD

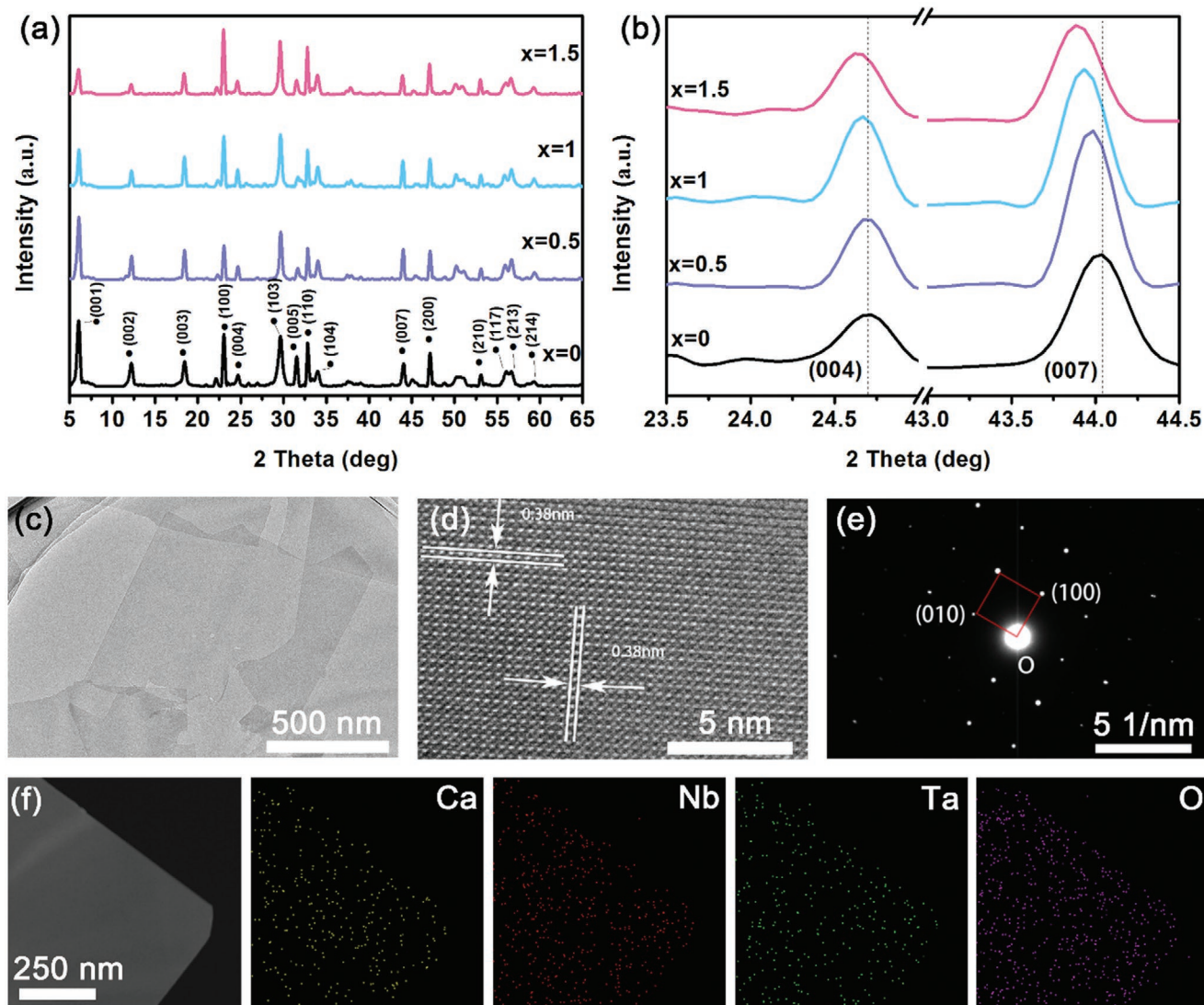


Figure 2. Crystal structure of the $\text{Ca}_2\text{Nb}_{3-x}\text{Ta}_x\text{O}_{10}$ nanosheets ($x = 0, 0.5, 1, 1.5$). a, b) XRD patterns of the $\text{HCa}_2\text{Nb}_{3-x}\text{Ta}_x\text{O}_{10}$ samples. c) TEM, d) HRTEM images, and e) SEAD pattern of the $\text{Ca}_2\text{Nb}_{2.5}\text{Ta}_{0.5}\text{O}_{10}$ nanosheets. f) Element mapping images of the $\text{Ca}_2\text{Nb}_{2.5}\text{Ta}_{0.5}\text{O}_{10}$ nanosheet.

patterns of the $\text{HCa}_2\text{Nb}_{3-x}\text{Ta}_x\text{O}_{10}$ samples derived from the proton exchange process match well with the standard data of $\text{HCa}_2\text{Nb}_3\text{O}_{10}$ (PDF#40-0884), with the highest three diffraction peaks 6.1° , 23.1° , 29.7° corresponding to (001), (100), (103) planes (Figure 2a). No second phase is observed in the XRD patterns of the $\text{HCa}_2\text{Nb}_{3-x}\text{Ta}_x\text{O}_{10}$ samples. Moreover, the diffraction peaks indexed to (004), (007) planes are shifted to smaller angles as the ratio of tantalum to niobium is increased as shown in Figure 2b. The successive shifts of diffraction peaks indicate that the obtained crystals are not mixtures of different phases, but $\text{HCa}_2\text{Nb}_{3-x}\text{Ta}_x\text{O}_{10}$ solid solutions with Ta atoms incorporated into the lattice of the crystal. Considering the same ionic radius of Nb^{5+} and Ta^{5+} (0.64 Å), Ta may substitute Nb to occupy the B-site in the perovskite slabs.^[27,30,31] Figure 2c–f displays a transmission microscopy (TEM) image, a high-resolution TEM image (HRTEM), selected area electron diffraction (SAED) pattern, and element mapping images for the $\text{Ca}_2\text{Nb}_{2.5}\text{Ta}_{0.5}\text{O}_{10}$ nanosheets, respectively. The TEM image

(Figure 2c) further illustrates the morphology of the materials, the 2D objects with the lateral size of $\approx 1 \mu\text{m}$ are identified as nanosheets. The HRTEM in Figure 2d exhibits the high crystallinity of the $\text{Ca}_2\text{Nb}_{2.5}\text{Ta}_{0.5}\text{O}_{10}$ nanosheets. Two sets of perpendicular lattice fringes with the interplanar spacing of 3.8 Å correspond to the (100) and (010) atomic planes of nanosheets. The SAED pattern (Figure 2e) indicates the single-crystal structure of the nanosheets and the marked directions correspond to (100) and (010) planes. The TEM characterization results are in agreement with the XRD data. Energy-dispersive X-ray spectroscopy (EDS) is utilized to explore the element distribution and atomic compositions of the $\text{Ca}_2\text{Nb}_x\text{Ta}_{3-x}\text{O}_{10}$ nanosheets. The element mapping images of the $\text{Ca}_2\text{Nb}_{2.5}\text{Ta}_{0.5}\text{O}_{10}$ nanosheets are displayed in Figure 2f, the uniform distribution of color blocks from Ta element further confirms the successful incorporation of Ta into the $\text{Ca}_2\text{Nb}_3\text{O}_{10}$ nanosheet lattice. Figure S3, Supporting Information, shows the crystal structure and the element distribution of the $\text{Ca}_2\text{Nb}_2\text{Ta}_1\text{O}_{10}$ and $\text{Ca}_2\text{Nb}_{1.5}\text{Ta}_{1.5}\text{O}_{10}$

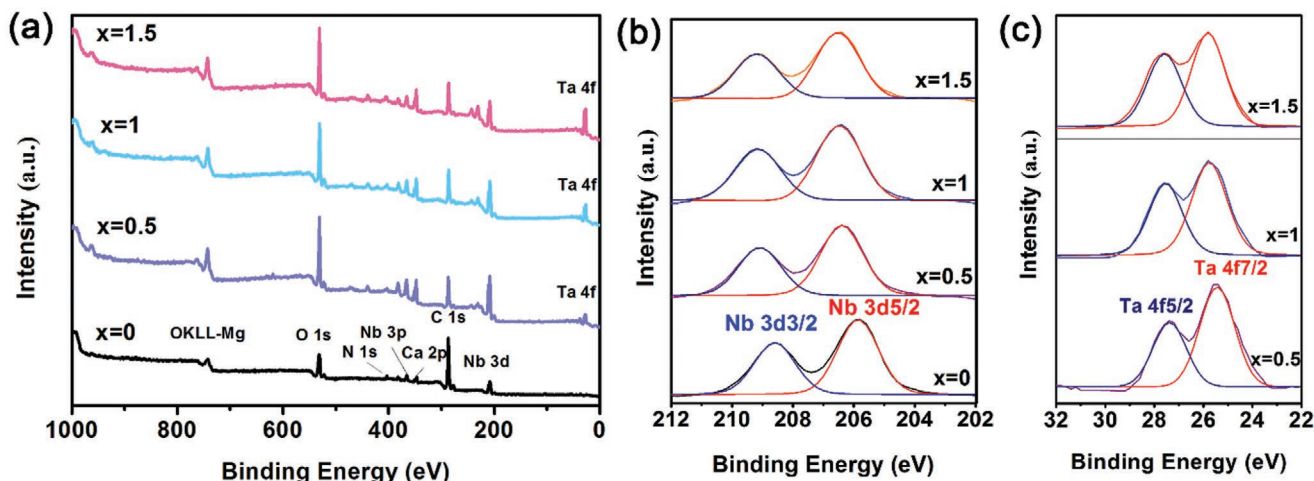


Figure 3. a) XPS survey spectra of the $\text{Ca}_2\text{Nb}_{3-x}\text{Ta}_x\text{O}_{10}$ nanosheets ($x = 0, 0.5, 1, 1.5$) and XPS spectra of b) Nb 3d, c) Ta 4f.

nanosheets, further proving the substitution of Ta atoms. The corresponding EDS spectrum (Figure S4 and Table S1, Supporting Information) gives the experimental Nb:Ta ratios for the $\text{Ca}_2\text{Nb}_{3-x}\text{Ta}_x\text{O}_{10}$ ($x = 0.5, 1, 1.5$) nanosheets, which are close to the target ratios 5:1, 2:1, 1:1, respectively.

X-ray photoelectron spectroscopy (XPS) is applied to study the surface elemental composition and chemical state of the $\text{Ca}_2\text{Nb}_{3-x}\text{Ta}_x\text{O}_{10}$ nanosheets. The survey spectra in Figure 3a reveal the dominant existence of Ca, Nb, O elements in the samples with any composition ratios. It is noteworthy that the characteristic peak of Ta element occurs when Ta atoms are incorporated into the $\text{Ca}_2\text{Nb}_3\text{O}_{10}$ nanosheets ($x > 0$). Detailed binding energy peaks of Ta and Nb elements are displayed in Figure 3b,c to illustrate their valence values. In Figure 3b, for the $\text{Ca}_2\text{Nb}_3\text{O}_{10}$ sample, the binding energy peaks located at 205.8 and 208.6 eV are attributed to Nb 3d 3/2 and Nb 3d 5/2, confirming the existence of Nb^{5+} in $\text{Ca}_2\text{Nb}_3\text{O}_{10}$. The incorporation of Ta into the nanosheet lattice brings a slight shift of Nb 3d peaks to higher binding energies, which is ascribed to the electronic structure change of Nb–O bonds. The explanation could be that the electronegativity difference between Ta and Nb leads to a change of the valence electron density, which influences the ejection of electrons from Nb^{5+} ions and thus results in the peak shift.^[32] The high resolution spectra of Ta 4f (Figure 3c) reveal the existence of Ta^{5+} in the $\text{Ca}_2\text{Nb}_{3-x}\text{Ta}_x\text{O}_{10}$ ($x = 0.5, 1, 1.5$) nanosheets, with the Ta 4f 7/2 peak centered on 27.4 eV and Ta 4f 5/2 located at 25.4 eV. And the surface element ratios are shown in Table S2, Supporting Information, which are also coincident with the target ratio. The XPS results further demonstrate the successful partial substitution of Ta for Nb in the $\text{Ca}_2\text{Nb}_3\text{O}_{10}$ nanosheets.

The $\text{Ca}_2\text{Nb}_{3-x}\text{Ta}_x\text{O}_{10}$ nanosheets are assembled on glass substrates by a simple drop coating method to form nanosheet films to fabricate PDs, and evaporation technique is applied to construct Cr/Au contacts with a fixed distance (10 μm) on the nanosheet films, as shown in Figure 4a. The absorption properties of the nanosheet films are characterized by UV–vis spectroscopy (Figure 4b). The absorption edges of all samples fall in the range of UV light. The negligible absorption over the visible range of these samples indicates they are potential

candidates for constructing UV PDs. The position of the absorption edge shifts to shorter wavelengths with the increase of the Ta content. The optical bandgaps of the nanosheets are determined by transforming their UV–vis absorbance spectra into Tauc plots using equation^[26]

$$(\alpha h\nu)^{1/2} = A(h\nu - E_g) \quad (1)$$

where h is Planck's constant, ν is the frequency, α is the absorption coefficient, and A is a proportionality constant. The inset image in Figure 4b illustrates the increase of bandgap energy from 3.43 eV ($x = 0$) to 3.65 eV ($x = 1.5$) corresponding to the blue shift of absorption curves. The wider bandgap could be ascribed to the change of conduction band brought by Ta incorporation, which will be discussed in the latter part. The photoelectric performance of the $\text{Ca}_2\text{Nb}_{3-x}\text{Ta}_x\text{O}_{10}$ PDs is investigated. Considering that the tunable bandgap of the material may influence the response wavelength range of the PDs, the spectral response performance is first explored by varying incident wavelength. Herein, the spectral responsivity (R_λ) is introduced to evaluate the spectral response performance of the $\text{Ca}_2\text{Nb}_{3-x}\text{Ta}_x\text{O}_{10}$ PDs, exhibiting the response sensitivity of a PD to optical signals within a wavelength range. R_λ is defined by the following formula

$$R_\lambda = \frac{I_{\text{ph}} - I_{\text{dark}}}{P_\lambda S} \quad (2)$$

where I_{ph} is the photocurrent, I_{dark} is the dark current, P_λ is the light power density, and S is the effective irradiation area. As shown in Figure 4c, the response wavelengths of all the PDs fall in the range of 250–400 nm, indicating their distinct UV light selectivity. It is noted that as the Ta content increases, the cut-off edge of the PDs shifts to a shorter wavelength with 350 nm for the $\text{Ca}_2\text{Nb}_3\text{O}_{10}$ PD and 330 nm for the $\text{Ca}_2\text{Nb}_{1.5}\text{Ta}_{1.5}\text{O}_{10}$ PD, respectively which is coincident with the absorbance curve of the material. Besides, the photoresponse peak is altered from 295 to 280 nm successively with the increase of Ta content, exhibiting a blue shift along with the cut-off edge. Significantly, the responsivities of all the PDs are enhanced by the

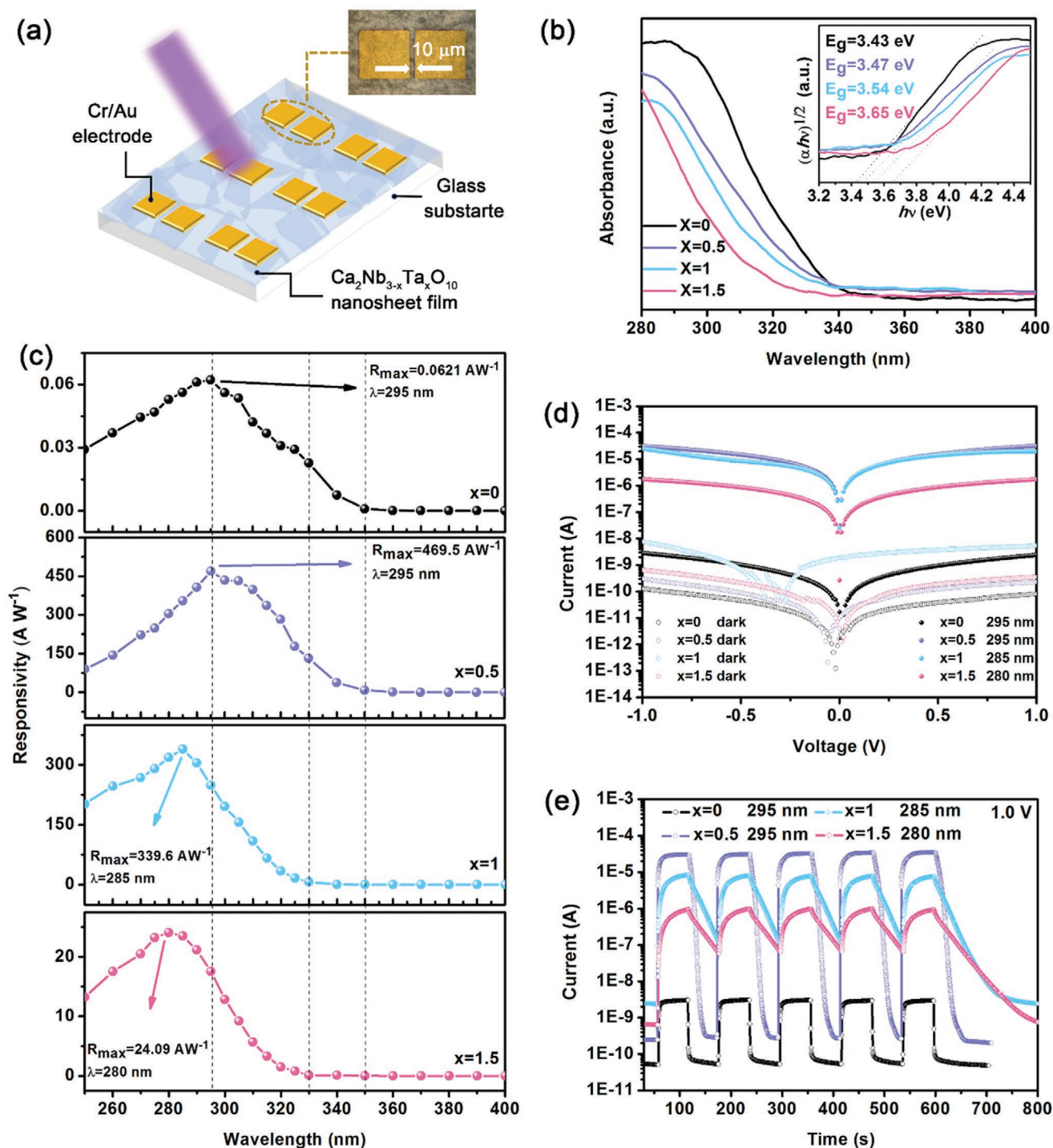


Figure 4. a) Schematic diagram of the $\text{Ca}_2\text{Nb}_{3-x}\text{Ta}_x\text{O}_{10}$ ($x = 0, 0.5, 1, 1.5$) nanosheet film PD. b) UV-vis absorption spectra of nanosheets, with the corresponding Tauc curves in the inset. c) The spectral responsivity of the PDs at 1.0 V bias. d) The semi-logarithmic I - V curves of the PDs in dark and under their specific wavelength illumination. e) I - t characteristics of the PDs at 1.0 V bias under their specific wavelength illumination.

substitution of Ta for Nb, with the maximum responsivity achieved in the $\text{Ca}_2\text{Nb}_{2.5}\text{Ta}_{0.5}\text{O}_{10}$ PD, reaching 469.5 A W^{-1} at 1.0 bias under 295 nm illumination, 7560-fold higher than that of dopant-free $\text{Ca}_2\text{Nb}_3\text{O}_{10}$ PD. Hence, the cut-off edge of the photodetectors could be regulated precisely by controlling the $\text{Ca}_2\text{Nb}_{3-x}\text{Ta}_x\text{O}_{10}$ composition parameter x , and the PDs are

more sensitive to UV irradiation with B-site cation Nb partially substituted by Ta. Figure 4d,e presents detailed I - V and I - t characteristics of the $\text{Ca}_2\text{Nb}_{3-x}\text{Ta}_x\text{O}_{10}$ nanosheet film-based PDs. As shown in Figure 4d, the pristine $\text{Ca}_2\text{Nb}_3\text{O}_{10}$ PD displays a low dark current of $\approx 80.1 \text{ pA}$ at 1.0 V bias and a photocurrent of $\approx 2.37 \text{ nA}$ under 295 nm illumination. Partial substitution of

Ta for Nb causes a relatively slight increase of dark current and a dramatic increase of photocurrent for all the $\text{Ca}_2\text{Nb}_{3-x}\text{Ta}_x\text{O}_{10}$ PDs, among which the $\text{Ca}_2\text{Nb}_{2.5}\text{Ta}_{0.5}\text{O}_{10}$ PD exhibits the most outstanding performance, yielding a boosted photocurrent of $\approx 31.4 \mu\text{A}$ at the same bias (1.0 V) and under the same illumination wavelength (295 nm) as the $\text{Ca}_2\text{Nb}_3\text{O}_{10}$ PD. The photocurrents of the $\text{Ca}_2\text{Nb}_2\text{Ta}_1\text{O}_{10}$ and $\text{Ca}_2\text{Nb}_{1.5}\text{Ta}_{1.5}\text{O}_{10}$ PDs remain at the microampere level, although the photocurrent appears to have a downward trend as the Ta content increases. The corresponding linear scale I - V curves are presented in Figure S5, Supporting information, to show the contact properties. Figure 4e displays the time-dependent current (I - t) curves of the PDs under their specific wavelength illumination on/off switching at 1.0 V bias. The $\text{Ca}_2\text{Nb}_3\text{O}_{10}$ and $\text{Ca}_2\text{Nb}_{2.5}\text{Ta}_{0.5}\text{O}_{10}$ PDs exhibit repeatable and stable on-off cycles from their dark current to their steady photocurrent upon illumination and back to their original dark state when the light is off. The on-off ratio of the $\text{Ca}_2\text{Nb}_{2.5}\text{Ta}_{0.5}\text{O}_{10}$ PD is $\approx 5.6 \times 10^4$, which is nearly 1000 times higher than that of pristine $\text{Ca}_2\text{Nb}_3\text{O}_{10}$ PD due to the boosted photocurrent. While for the $\text{Ca}_2\text{Nb}_2\text{Ta}_1\text{O}_{10}$ and $\text{Ca}_2\text{Nb}_{1.5}\text{Ta}_{1.5}\text{O}_{10}$ PDs, the conductance baselines are not fully recovered in the same time interval after switching off the light. Although the photocurrent of the $\text{Ca}_2\text{Nb}_2\text{Ta}_1\text{O}_{10}$ PD under 285 nm UV illumination at 1.0 V bias is very high, its slow decay speed results in its relatively low on-off ratio, and the further increase of Ta content leads to remarkable decay of the photodetecting performance for the $\text{Ca}_2\text{Nb}_{1.5}\text{Ta}_{1.5}\text{O}_{10}$ PD.

It is noteworthy that the $\text{Ca}_2\text{Nb}_{2.5}\text{Ta}_{0.5}\text{O}_{10}$ PD shows the optimal responsivity and acceptable response speed among all the PDs. Herein, the photodetecting performance of the $\text{Ca}_2\text{Nb}_{2.5}\text{Ta}_{0.5}\text{O}_{10}$ PD is systematically investigated as shown in Figure 5. Figure 5a displays the current-voltage (I - V) characteristics of the PD in dark and under 280, 295, and 350 nm UV illumination in semilogarithmic coordinates. The I - V curves indicate its effective response to incident UV light, with high photocurrents under 280 and 295 nm at 1.0 V bias. Figure 5b illustrates the I - t curves of the PD under 295 nm UV on/off switching at various bias voltage 1.0, 0.5, and 0.1 V. The PD exhibits a high stable photocurrent of $\approx 19.8 \mu\text{A}$ and a high on-off ratio of over 10^5 at 0.5 V bias. When the bias voltage is lowered to 0.1 V, the PD still shows excellent performance with a stable photocurrent of $\approx 4.2 \mu\text{A}$ and high repeatability to UV switching, exhibiting its potential in low-driving-voltage photodetection. Apart from the responsivity mentioned above, in order to further evaluate the performance, two important parameters detectivity (D^*) and external quantum efficiency (EQE) are introduced. Detectivity illustrates the sensitivity of the PD to weak signals from the noise environment, in which the dark current is the major noise. It can be calculated from the following formula

$$D^* = \frac{R_\lambda}{\left(\frac{2eI_d}{s}\right)^{\frac{1}{2}}} \quad (3)$$

where R_λ represents the responsivity at specific wavelength, e is the elementary charge, I_d is the dark current, and S is the effective area under irradiation. EQE is the ratio of photogenerated carriers to the number of incident photons,

indicating the photoelectric conversion efficiency of the PD. It can be calculated as

$$\text{EQE} = \frac{hc}{e\lambda} R_\lambda \quad (4)$$

where h , c , and λ refer to the Planck constant, light speed, and wavelength. Figure 5c shows the calculated detectivity and EQE as a function of wavelength at 1.0 V bias. The PD remains high detectivity of $>10^{13}$ Jones in the wavelength range of 250–330 nm and reaches the highest value under 295 nm UV illumination (7.65×10^{13} Jones), indicating its outstanding photoresponse to weak UV signals. The PD also exhibits excellent photoelectric conversion efficiency with EQE up to $1.97 \times 10^5\%$ under 295 nm illumination. To precisely illustrate the response speed of the $\text{Ca}_2\text{Nb}_{2.5}\text{Ta}_{0.5}\text{O}_{10}$ PD, a quick response system constructed with a pulsed YAG:Nd laser and an oscilloscope is applied to record the time-resolved pulse response curve of the PD. One period of pulse response repetitions at 1.0 V bias is displayed in Figure 5d. The rise time from 10% to 90% (T_r) is ≈ 0.9 ms, indicating its fast rise response upon irradiation, while its recovery performance is not that outstanding but acceptable with a decay time from 90% to 10% (T_d) estimated to be 152 ms. The influence of the incident light power density on the photoresponse behaviors of the $\text{Ca}_2\text{Nb}_{2.5}\text{Ta}_{0.5}\text{O}_{10}$ is also investigated at 1.0 V bias under 295 nm illumination (Figure 5e). It is shown that with the incident light power densities ranging from 0.101 to 1.396 mW cm^{-2} , the photocurrent of the PD is positively related to the power density. Generally, the photogeneration efficiency of charge carriers and the absorbed photon flux follow a proportional relationship, which could be determined by the following power law formula:

$$I_{\text{ph}} = AP^\theta \quad (5)$$

where I_{ph} is the photocurrent, P is the incident light power density, A is a constant for a certain wavelength, and the exponent θ exhibits the response relationship ($0.5 < \theta < 1$). Figure 5f illustrates the curve fitted through the Equation (5), and the value of θ turns out to be 0.989, 0.988, and 0.922 at 1.0, 0.5, and 0.1 V bias respectively, indicating the near-linear dependence of this PD. Moreover, stability, an important requirement to evaluate the performance of a PD,^[33,34] is also satisfied in the $\text{Ca}_2\text{Nb}_{3-x}\text{Ta}_x\text{O}_{10}$ PD. The $\text{Ca}_2\text{Nb}_3\text{O}_{10}$ nanosheets film PD exhibits long-term stability over 200 days under ambient condition.^[19] No obvious impact of partial substitution on device stability is observed during our test. In addition, the photodetecting performance of the PDs based on $\text{Ca}_2\text{Nb}_{3-x}\text{Ta}_x\text{O}_{10}$ nanosheets with other composition ratios ($x = 0$, $x = 1$, $x = 1.5$) is summarized in Figures S6–S8, Supporting Information.

Derived from the results mentioned above, it can be concluded that the substitution of Ta heteroatoms brings the material tunable bandgap and influences its photoelectric properties, providing the precise control of the response spectral range and optimized responsivity for the PDs. Here, the plausible physical mechanisms are discussed in detail. The atomic schematic of the $\text{Ca}_2\text{Nb}_{3-x}\text{Ta}_x\text{O}_{10}$ nanosheets is shown in Figure 6a. As has been previously described, the nanosheets are exfoliated from layered DJ perovskites $\text{KCa}_2\text{Nb}_{3-x}\text{Ta}_x\text{O}_{10}$, with K cations

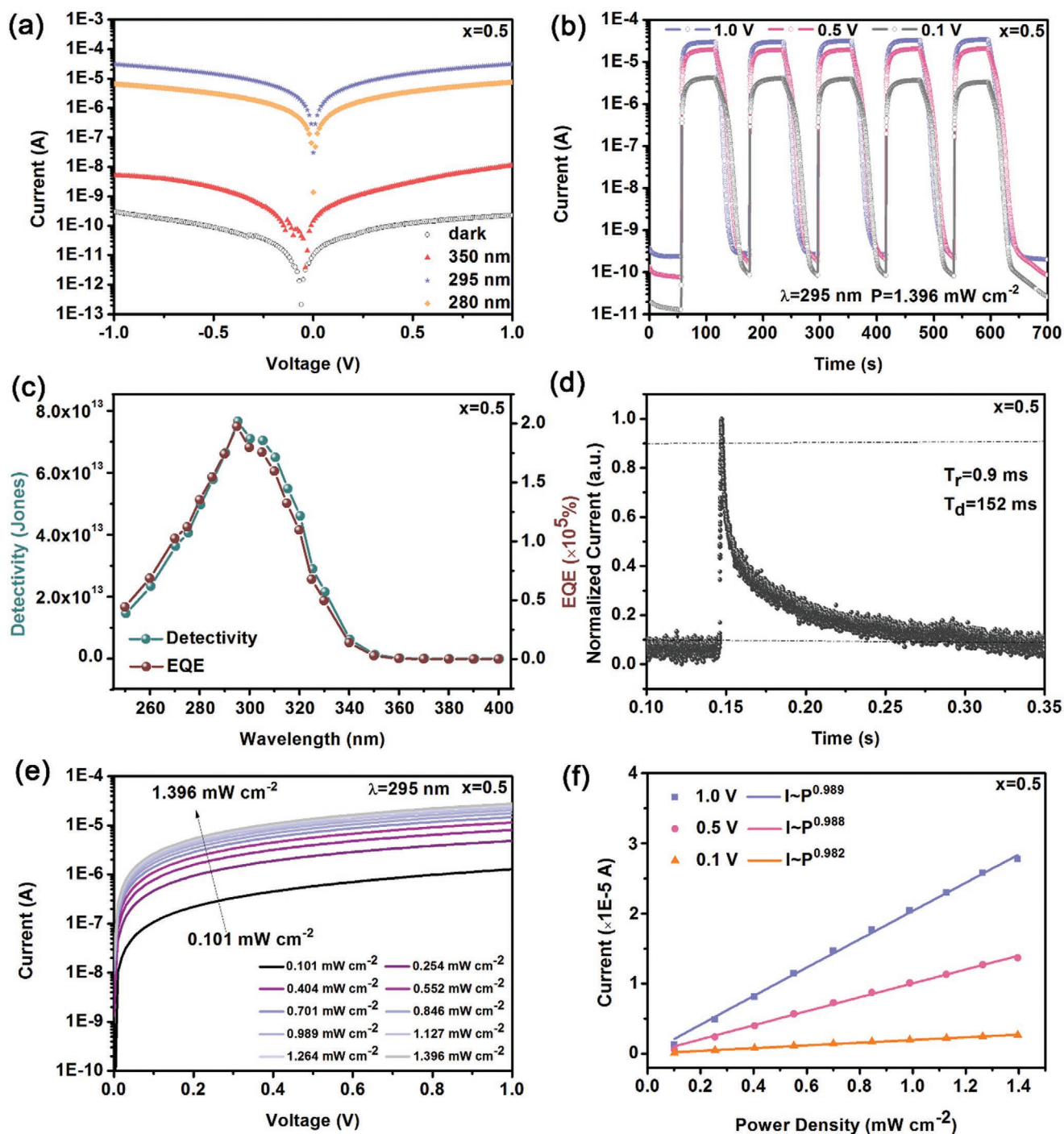


Figure 5. Photodetecting performance of the $\text{Ca}_2\text{Nb}_{2.5}\text{Ta}_{0.5}\text{O}_{10}$ PD. a) I - V curves in dark and under UV light illumination. b) I - t curves under 295 nm illumination at 1.0, 0.5, and 0.1 V bias. c) Calculated detectivity and EQE curve of 250–400 nm at 1.0 V bias. d) Estimated rise and decay time from single pulse response curve. e) I - V curves under 295 nm illumination with various incident power densities. f) Photocurrent as a function of incident power density and their corresponding power law fitting curves under 295 nm illumination at 1.0, 0.5, and 0.1 V bias.

eliminated, leaving negatively charged thin $\text{Ca}_2\text{Nb}_{3-x}\text{Ta}_x\text{O}_{10}$ slabs, whose thickness depends on the number of BO_6 octahedra in c -axis ($n = 3$).^[8] Successful incorporation of Ta atoms into the lattice of calcium niobate nanosheets has been confirmed from the crystal characterization results. Considering

the same ionic radius of Nb^{5+} and Ta^{5+} (0.64 Å), Ta atoms are proposed to occupy Nb sites (B-site of DJ perovskite oxides) in the host perovskite layer and form TaO_6 octahedra.^[27,30,35,36] As has been mentioned above, the optical light absorption edge of the $\text{Ca}_2\text{Nb}_{3-x}\text{Ta}_x\text{O}_{10}$ nanosheets exhibits a blue shift and the

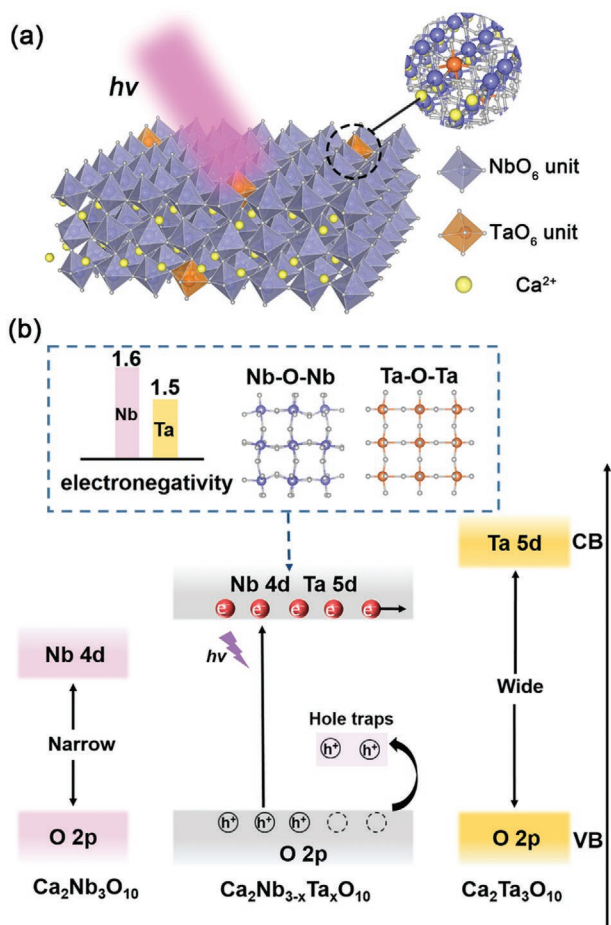


Figure 6. a) Atomic schematic of the $\text{Ca}_2\text{Nb}_{3-x}\text{Ta}_x\text{O}_{10}$ nanosheet. b) Schematic demonstration interpreting the plausible mechanism for the tunable bandgap and the significant enhancement of the photo-detecting performance.

estimated band gaps become wider with the gradual increase of Ta atomic composition. Figure 6b roughly describes the change of the band structures of $\text{Ca}_2\text{Nb}_{3-x}\text{Ta}_x\text{O}_{10}$. The increase of the band gap energies could be ascribed to the shift of the conduction band edge. Scaife reported that the band structures of metal oxides containing d^0 -early transition metal cations consist of oxygen 2p orbitals and transition metal d orbitals.^[37] The valence band potentials of the samples with different composition ratios are similar because they are all determined by the O 2p orbitals and six O^{2-} coordinate to Nb^{5+} or Ta^{5+} with identical ionic radius.^[38] Whereas, the conduction band potential should be influenced by the incorporation of Ta atoms. Nb 4d orbitals and Ta 5d orbitals contribute most to the conduction band in $\text{Ca}_2\text{Nb}_3\text{O}_{10}$ and $\text{Ca}_2\text{Ta}_3\text{O}_{10}$, respectively, and the conduction band edge of $\text{Ca}_2\text{Ta}_3\text{O}_{10}$ is higher, resulting in its wider band gap. It has been reported that the electronegativity of the B-site cation has a significant effect on the band gap of the d^0 transition metal oxide perovskites, and the band gap energy increases sensitively with the decrease of the electronegativity ($X_{\text{Nb}} > X_{\text{Ta}}$).^[28] Therefore, partial substitution of Ta for Nb brings successive shifts of conduction band edge to higher energies, which is responsible for the tunable bandgap of

the $\text{Ca}_2\text{Nb}_{3-x}\text{Ta}_x\text{O}_{10}$ nanosheets and the corresponding precise control of spectral response of the PDs.

Apparently, the concentration of Ta atoms affects the photo-detecting performance of the $\text{Ca}_2\text{Nb}_{3-x}\text{Ta}_x\text{O}_{10}$ PDs. All the Ta substituted PDs show increased photocurrent and enhanced responsivity compared to the pristine $\text{Ca}_2\text{Nb}_3\text{O}_{10}$ PD, meanwhile, at the cost of response speed. The optimized responsivity can be attributed to the enhanced photoconductive gain induced by the introduction of trap states, and the trap states mainly come from the point defects introduced by the B-site substitution. The responsivity R_p of a photoconductive detector has a relationship with the photoconductive gain G , which can be expressed by^[39,40]

$$R_p = R_0 \times G = \frac{\eta e}{h\nu} \times G \quad (6)$$

where R_0 is the intrinsic responsivity, η is the quantum efficiency, e is electron charge, h is the Planck constant, and ν is the frequency of the light. And the photoconductive gain is given by

$$G = \frac{\tau_c}{\tau_t} \quad (7)$$

where τ_c is the carrier lifetime, τ_t is the carrier transit time.^[41] The impurities and defects in low dimensional materials tend to act as trap centers rather than recombination centers due to the large specific surface area and limited dimension.^[42] If the minority carrier trapping effect is induced by them, the lifetime of the photogenerated carriers will be significantly prolonged, contributing to the high photoconductive gain, according to Equation (7).^[41] In this work, considering the differences in the crystal structure and physicochemical of Ta and Nb atoms, the substitution of Ta for Nb inevitably brings point defects to this 2D material. The chemical bonding character of B—O—B can be notably affected by the B site cation in DJ perovskite,^[43] as shown in the B—O—B bond schematic for $\text{KCa}_2\text{Nb}_3\text{O}_{10}$ and $\text{KCa}_2\text{Ta}_3\text{O}_{10}$ (Figure 6b). The Ta—O bond is less covalent than that of the Nb—O bond, and the bond angle of B—O—B is also influenced.^[43] Therefore, the substitution of Ta might introduce the distortion of BO_6 octahedra in the $\text{Ca}_2\text{Nb}_{3-x}\text{Ta}_x\text{O}_{10}$ crystal,^[28,31] coincident with the peak shifts in XRD patterns. Moreover, although Ta and Nb atoms own the same number of valence electrons, the electronegativity difference between them would possibly introduce an in-gap defect level, and the lower electronegativity of Ta atom ($X_{\text{Nb}} = 1.6$, $X_{\text{Ta}} = 1.5$) endows it with the capability of trapping holes.^[44] As shown in Figure 6b, the illumination with photon energy above their bandgap results in the generation of electron-hole pairs whose holes are rapidly captured into defect-induced traps. When photogenerated electrons drift through the photoconductor to reach the anode within τ_t , the electrons in the photoconductor are continuously replenished by the cathode to maintain the charge neutrality. Multiple electrons circulate after an electron-hole pair is generated by a photon. This process repeats as long as the holes remain in the trap states. The long lifetime (τ_c) of the trapped holes leads to the greatly enhanced photoconductive gain and thus optimized responsivity in Ta-substituted PDs according to the equations mentioned above.^[40,42,45]

Nevertheless, when the Ta content is increased to above 0.5, the responsivity exhibits a downward trend instead. We propose the decline of the responsivity can be ascribed to the following several factors. The excess substitution brings additional scattering, which would reduce the mobility of the carriers, prolong the carrier transit time τ_t and suppress the charge collection efficiency.^[46] In addition, the excess defects might act as recombination centers, leading to the recombination of a fraction of photogenerated carriers to some extent. It is also revealed that the bond character of the B–O–B in this kind of perovskites would influence the movement of the photogenerated carriers considering the delocalization of electron–hole pairs, which implies the significant change of the crystal structure induced by high concentration substitution has the possibility to suppress the carrier movement.^[28] Therefore, the optimization of responsivity can only be achieved on the basis of a rational substitution concentration. In terms of the response speed, enhanced photoconductive gain induced by the trap states inevitably limits the decay speed.^[42] The decay time of the photoconductor is determined by the lifetime of the carriers and an additional decay time required for emptying traps.^[22] The existence of the long-lived and deep-trapped carriers therefore results in the decline of the response speed with the increase of the Ta content in the $\text{Ca}_2\text{Nb}_{3-x}\text{Ta}_x\text{O}_{10}$ PDs. Overall, the $\text{Ca}_2\text{Nb}_{2.5}\text{Ta}_{0.5}\text{O}_{10}$ PD exhibit the optimal photodetecting performance among all the samples, achieving the highest responsivity originated from the minority carrier trapping effect combined with the efficient carrier transport of the majority carriers,^[45] meanwhile, with an acceptable response speed. Hence, based on the plausible mechanism of defect-induced photoconductive gain, it is possible to tune the response of the PDs and establish a suitable balance to achieve excellent responsivity and acceptable response speed simultaneously via careful control over the composition ratio.

3. Conclusion

In conclusion, B-site substituted calcium niobate $\text{Ca}_2\text{Nb}_{3-x}\text{Ta}_x\text{O}_{10}$ ($x = 0, 0.5, 1, 1.5$) nanosheets are prepared by calcination and subsequent multi-step soft chemical exfoliation. XRD and TEM results confirm the high crystallinity of the nanosheets and prove the successful partial substitution of Ta for Nb. The PDs based on these nanosheets with various composition ratios are fabricated and investigated. The control over the Ta content can tailor the band gap of the nanosheets due to the shifts of conduction band edge to higher energies, and thus control the spectral response range of the PDs precisely. All the Ta-substituted PDs show increased photocurrent and enhanced responsivity compared to the pristine $\text{Ca}_2\text{Nb}_3\text{O}_{10}$ PD, among which the $\text{Ca}_2\text{Nb}_{2.5}\text{Ta}_{0.5}\text{O}_{10}$ PD exhibits the optimal photodetecting performance with a photocurrent of 31.4 μA , a high on–off ratio of 5.6×10^4 and a boosted responsivity of 469.5 A W^{-1} at 1.0 V bias under 295 nm illumination, which is over 7000-fold higher than that of the pristine $\text{Ca}_2\text{Nb}_3\text{O}_{10}$ PD. We propose that the significantly optimized responsivity is ascribed to the enhanced photoconductive gain that mainly originates from the introduction of the trap states by the B-site substitution. The trap-induced prolonged lifetime of the

minority carriers, combined with the efficient carrier transport of the majority carriers contributes to the outperformance of the $\text{Ca}_2\text{Nb}_{2.5}\text{Ta}_{0.5}\text{O}_{10}$ PD among all the samples in terms of the responsivity. Besides, although enhanced responsivity produced by the long-lived carriers inevitably limits the response speed, the suitable composition ratio makes the $\text{Ca}_2\text{Nb}_{2.5}\text{Ta}_{0.5}\text{O}_{10}$ PD achieve a high responsivity and an acceptable response speed simultaneously. Thus, the rational control of the substitution on the B-site tailors the band gap and modulates the charge-carrier behaviors in 2D perovskite oxides, which provides an effective avenue for achieving high-performance PDs with excellent responsivity and tunable spectral response.

4. Experimental Section

Synthesis of $\text{Ca}_2\text{Nb}_{3-x}\text{Ta}_x\text{O}_{10}$ Nanosheets: The synthesis of the $\text{Ca}_2\text{Nb}_{3-x}\text{Ta}_x\text{O}_{10}$ nanosheets consists of three stages: solid state reaction, proton exchange, and exfoliation. The bulk layered perovskite $\text{KCa}_2\text{Nb}_{3-x}\text{Ta}_x\text{O}_{10}$ was synthesized by solid state reaction using K_2CO_3 (99.99% Alladin), CaCO_3 (99.99% Alladin), Nb_2O_5 (99.99% Alladin), Ta_2O_5 (99.99% Alladin) with a molar ratio of K/Ca/Nb/Ta = 1.1/2/3–x/x ($x = 0, 0.5, 1, 1.5$), where an excess of K_2CO_3 (10%) was added to compensate for the loss of K during high temperature calcination. The precursor mixture was ground thoroughly for 0.5 h before calcination at 1100 °C for 10 h in air. In proton exchange process, the obtained $\text{KCa}_2\text{Nb}_{3-x}\text{Ta}_x\text{O}_{10}$ perovskite powder was stirred in 3 M HNO_3 solution for 4 days to replace K ions with proton. The protonated powder ($\text{HCa}_2\text{Nb}_{3-x}\text{Ta}_x\text{O}_{10}$) was then washed several times with distilled water and dried at 80 °C in air. The exfoliation process was completed by using TBAOH (prepared from 25% aqueous solution, tetrabutylammonium). The obtained powder from the second stage was dispersed in 50 mL of aqueous solution containing an equimolar amount of TBAOH and then mechanically shaken for 1 week to obtain the $\text{Ca}_2\text{Nb}_{3-x}\text{Ta}_x\text{O}_{10}$ nanosheets. The nanosheets were finally washed several times with distilled water and collected by centrifugation.

Characterization of $\text{Ca}_2\text{Nb}_{3-x}\text{Ta}_x\text{O}_{10}$ Nanosheets: The morphology characterization of exfoliated $\text{Ca}_2\text{Nb}_{3-x}\text{Ta}_x\text{O}_{10}$ was carried out by SEM (Zeiss Sigma). AFM (Bruker Multimode Catalyst) was used to measure the thickness of the nanosheets. The microstructure and phase analysis of the $\text{HCa}_2\text{Nb}_{3-x}\text{Ta}_x\text{O}_{10}$ powder samples were investigated by XRD (Bruker D8A25) with Cu $K\alpha$ radiation ($\lambda = 1.5405 \text{ \AA}$). HRTEM (JEM-1400 plus) was utilized for further characterization of the morphology and the crystal structure, as well as the element mapping. The investigation of surface elemental composition and chemical state was carried out on XPS (PHI 5000C ESCA). The optical properties were analyzed by UV–vis spectra utilizing a UV–vis spectrophotometer (Hitachi, U-3900H).

Photoelectric Measurements: The $\text{Ca}_2\text{Nb}_{3-x}\text{Ta}_x\text{O}_{10}$ nanosheet film-based photodetector on glass substrate were fabricated via a simple drop coating method and vacuum evaporation of Cr/Au (10/60 nm) contacts, which was patterned by a shadow mask. The measurements were carried out in air with a temperature of about 25 °C and a humidity of 50–60% rh. All the photoelectric behaviors were investigated by a semiconductor characterization system (Keithley 4200, USA). A 450 W Xenon lamp assembled with a monochromator was used as the light source and the measurement of the light power density was conducted on a NOVA II power meter (OPHIR Photonics). A system consisting of a digital oscilloscope (Tektronix DPO 5140B) and a 355 nm Nd:YAG pulsed laser was utilized to characterize the pulse response property.

Supporting Information

Supporting Information is available from the Wiley Online Library or from the author.

Acknowledgements

The work was supported by National Natural Science Foundation of China (No. 1201101405 and 51872050), Ministry of Education Joint Fund for Equipment Pre-Research (No. 6141A02033241), and Science and Technology Commission of Shanghai Municipality (No. 19520744300 and 18520744600). Part of the research was carried out in Fudan Nanofabrication Laboratory. D.V.S. gratefully acknowledge the financial support from the Russian Science Foundation (No. 21-49-00039).

Conflict of Interest

The authors declare no conflict of interest.

Data Availability Statement

Data sharing is not applicable to this article as no new data were created or analyzed in this study.

Keywords

Ca₂Nb_{3-x}Ta_xO₁₀, high responsivity, perovskite nanosheets, tunable bandgap, UV photodetectors

Received: February 10, 2021

Revised: February 21, 2021

Published online: March 9, 2021

- [1] M. Dion, M. Ganne, M. Tournoux, *Mater. Res. Bull.* **1981**, 16, 1429.
 [2] Y. Kobayashi, M. Tian, M. Eguchi, T. E. Mallouk, *J. Am. Chem. Soc.* **2009**, 131, 9849.
 [3] I. Hase, Y. Nishihara, *Phys. Rev. B* **1998**, 58, R1707.
 [4] Y. Moritomo, A. Asamitsu, H. Kuwahara, Y. Tokura, *Nature* **1996**, 380, 141.
 [5] I. Grinberg, D. V. West, M. Torres, G. Y. Gou, D. M. Stein, L. Y. Wu, G. N. Chen, E. M. Gallo, A. R. Akbashev, P. K. Davies, J. E. Spanier, A. M. Rappe, *Nature* **2013**, 503, 509.
 [6] S. Ida, Y. Okamoto, M. Matsuka, H. Hagiwara, T. Ishihara, *J. Am. Chem. Soc.* **2012**, 134, 15773.
 [7] F. F. Xu, Y. Ebina, Y. Bando, T. Sasaki, *J. Phys. Chem. B* **2003**, 107, 9638.
 [8] R. Ma, T. Sasaki, *Adv. Mater.* **2010**, 22, 5082.
 [9] D. Lu, G. Lv, Z. Xu, Y. Dong, X. Ji, Y. Liu, *J. Am. Chem. Soc.* **2020**, 142, 11114.
 [10] H. Wu, X. Lian, S. Tian, Y. Zhang, M. Qin, Y. Zhang, F. Wang, X. Lu, G. Wu, H. Chen, *Sol. RRL* **2020**, 4, 2000087.
 [11] H. Wang, Z. Qin, J. Xie, S. Zhao, K. Liu, X. Guo, G. Li, X. Lu, K. Yan, J. Xu, *Small* **2020**, 16, 2003098.
 [12] L. Chang, M. A. Holmes, M. Waller, F. E. Osterloh, A. J. Moule, *J. Mater. Chem.* **2012**, 22, 20443.
 [13] C.-H. Chen, Z. Li, Q. Xue, Y.-A. Su, C.-C. Lee, H.-L. Yip, W.-C. Chen, C.-C. Chueh, *Org. Electron.* **2019**, 75, 105400.
 [14] Y. Shang, Y. Liao, Q. Wei, Z. Wang, B. Xiang, Y. Ke, W. Liu, Z. Ning, *Sci. Adv.* **2019**, 5, eaaw8072.
 [15] S. Li, Y. Zhang, W. Yang, H. Liu, X. S. Fang, *Adv. Mater.* **2020**, 32, 1905443.
 [16] H. P. Wang, S. Y. Li, X. Y. Liu, Z. F. Shi, X. S. Fang, J. H. He, *Adv. Mater.* **2021**, 33, 2003309.
 [17] O. C. Compton, E. C. Carroll, J. Y. Kim, D. S. Larsen, F. E. Osterloh, *J. Phys. Chem. C* **2007**, 111, 14589.
 [18] E. C. Carroll, O. C. Compton, D. Madsen, F. E. Osterloh, D. S. Larsen, *J. Phys. Chem. C* **2008**, 112, 2394.
 [19] Y. Zhang, S. Li, Z. Li, H. Liu, X. Liu, J. Chen, X. S. Fang, *Nano Lett.* **2021**, 21, 382.
 [20] L. Yin, P. He, R. Cheng, F. Wang, F. Wang, Z. Wang, Y. Wen, J. He, *Nat. Commun.* **2019**, 10, 4133.
 [21] W. Ouyang, F. Teng, J.-H. He, X. S. Fang, *Adv. Funct. Mater.* **2019**, 29, 1807672.
 [22] J. Jiang, C. Ling, T. Xu, W. Wang, X. Niu, A. Zafar, Z. Yan, X. Wang, Y. You, L. Sun, J. Lu, J. Wang, Z. Ni, *Adv. Mater.* **2018**, 30, 1804332.
 [23] H. Chang, Z. Sun, M. Saito, Q. Yuan, H. Zhang, J. Li, Z. Wang, T. Fujita, F. Ding, Z. Zheng, F. Yan, H. Wu, M. Chen, Y. Ikuhara, *ACS Nano* **2013**, 7, 6310.
 [24] J. Yao, G. Yang, *Nanoscale* **2020**, 12, 454.
 [25] K. Maeda, M. Eguchi, T. Oshima, *Angew. Chem., Int. Ed.* **2014**, 53, 13164.
 [26] P. Xu, T. J. Milstein, T. E. Mallouk, *ACS Appl. Mater. Interfaces* **2016**, 8, 11539.
 [27] Y. Okamoto, S. Ida, J. Hyodo, H. Hagiwara, T. Ishihara, *J. Am. Chem. Soc.* **2011**, 133, 18034.
 [28] G. Zhang, G. Liu, L. Wang, J. T. S. Irvine, *Chem. Soc. Rev.* **2016**, 45, 5951.
 [29] Y.-H. Kim, H.-J. Kim, M. Osada, B.-W. Li, Y. Ebina, T. Sasaki, *ACS Appl. Mater. Interfaces* **2014**, 6, 19510.
 [30] Q. Liu, Q. Zhang, L. Zhang, W.-L. Dai, *J. Mater. Sci. Technol.* **2020**, 54, 20.
 [31] H. Kato, A. Kudo, *J. Photochem. Photobiol., A* **2001**, 145, 129.
 [32] Z. Li, Y. Chen, P. Zhu, N. Ji, X. Duan, H. Jiang, *RSC Adv.* **2017**, 7, 53111.
 [33] Z. Q. Li, Z. L. Li, Z. F. Shi, X. S. Fang, *Adv. Funct. Mater.* **2020**, 30, 2002634.
 [34] M. Y. Liao, *Funct. Diamond* **2021**, 1, 29.
 [35] R. R. Sun, X. Y. Qin, L. L. Li, D. Li, N. N. Wang, J. Zhang, Q. Q. Wang, *J. Appl. Phys.* **2012**, 112, 124904.
 [36] H. J. Jo, E. S. Kim, *J. Eur. Ceram. Soc.* **2016**, 36, 1399.
 [37] D. E. Scaife, *Sol. Energy* **1980**, 25, 41.
 [38] Y. M. Akihiko Kudo, *Catal. Surv. Asia* **2003**, 7, 31.
 [39] X. Zhou, X. Hu, B. Jin, J. Yu, K. Liu, H. Li, T. Zhai, *Adv. Sci.* **2018**, 5, 1800478.
 [40] E. Liu, M. Long, J. Zeng, W. Luo, Y. Wang, Y. Pan, W. Zhou, B. Wang, W. Hu, Z. Ni, Y. You, X. Zhang, S. Qin, Y. Shi, K. Watanabe, T. Taniguchi, H. Yuan, H. Y. Hwang, Y. Cui, F. Miao, D. Xing, *Adv. Funct. Mater.* **2016**, 26, 1938.
 [41] G. Konstantatos, L. Levina, A. Fischer, E. H. Sargent, *Nano Lett.* **2008**, 8, 1446.
 [42] H. Fang, W. Hu, *Adv. Sci.* **2017**, 4, 1700323.
 [43] T. T. Kenji Toda, Z. Ye, M. Sato, Y. Hinatsu, *Mater. Res. Bull.* **1999**, 34, 971.
 [44] T. Kanai, M. Satoh, I. Miura, *J. Am. Ceram. Soc.* **2008**, 91, 456.
 [45] G. Konstantatos, E. H. Sargent, *Appl. Phys. Lett.* **2007**, 91, 173505.
 [46] Y. Zhang, X. Chen, Y. Xu, H. Gong, Y. Yang, F.-F. Ren, B. Liu, S. Gu, R. Zhang, J. Ye, *ACS Appl. Electron. Mater.* **2020**, 2, 808.